Acta Materialia 241 (2022) 118377

Contents lists available at ScienceDirect

Acta Materialia

journal homepage: www.elsevier.com/locate/actamat

Full length article

The role of mechanical loading in bcc-hcp phase transition: tension-compression asymmetry and twin formation

Amir Hassan Zahiri[1], Eduardo Vitral[1], Jamie Ombogo, Mehrab Lotfpour, Lei Cao*

Department of Mechanical Engineering, University of Nevada, Reno, Reno, NV 89557, USA

ARTICLE INFO

Article history:
Received 3 June 2022
Revised 1 September 2022
Accepted 21 September 2022
Available online 26 September 2022

Keywords:
Martensite phase transformation
Twinning
Tension-compression asymmetry
Molecular dynamics

ABSTRACT

In response to temperature or pressure changes, many body-centered cubic (bcc) materials undergo martensitic bcc-hcp phase transformation, which is known to produce rich martensite microstructure with internal twins. Mechanical loading is also known to have a huge impact on martensitic phase transformation. In this work, we integrate atomistic simulations with theoretical calculations to investigate the effect of mechanical loading on the martensite microstructure. The calculations of deformation gradients and transformation strains reveal that the $\{10\bar{1}1\}$ transformation twins and $\{10\bar{1}2\}$ transformation twins are favored by opposite loading directions. Furthermore, the initial {112} twin in the bcc phase is transformed into $\{11\bar{2}2\}$ and $\{11\bar{2}1\}$ twins after the phase transformation. The results reveal the critical role of mechanical loading in the formation of the specific transformation twinning, which could offer a novel strategy to engineer twin microstructure using designed thermomechanical processing.

1. Introduction

At high temperatures, many materials exist in more open structures such as the body-centered cubic (bcc) structure, while at low temperatures they transform into more close-packed structures such as the hexagonal close-packed (hcp) structure. It is well known that bcc-hcp solid-state phase transformations can be induced by temperature or pressure changes, and exist in many materials such as iron [1,2], titanium (Ti), zirconium, and many alloys [3–5]. Bcc-hcp phase transformation often occurs readily through collective atomic movements over small distances and is thus characterized as martensitic phase transformation. The orientation relation involved in a bcc-hcp phase transformation depends on the phase transformation mechanisms [6–8]. The most well-known Burgers mechanism [9] comprises a shear along the $(1\bar{1}2)_{bcc}$ plane, which converts the 70.53° angle between two $\langle 111\rangle_{bcc}$ directions in the $(110)_{bcc}$ plane to the 60° angle between two $\langle 11\bar{2}0\rangle_{hcp}$ directions. The shear is **accompanied** by a shuffle of alternating $(110)_{bcc}$ planes in the opposite $[1\bar{1}0]_{bcc}$ directions [10–12]. Specifically, the Burgers mechanism has the planar correspondence of $(01\bar{1})_{bcc} \parallel (0001)_{hcp}$ and the directional correspondence of $[1\bar{1}1]_{bcc} \parallel [11\bar{2}0]_{hcp}$. Another bcc-hcp phase transformation mechanism, the Pitsch–Schrader (PS) mechanism, has been observed experimentally in iron-, zirconium-, and magnesium-alloy systems [13–15]. It has the same planar correspondence but a different directional correspondence of $[001]_{bcc} \parallel [2\bar{1}\bar{1}0]_{hcp}$. Other less discussed mechanisms include the Potter and the Rong–Dunlop mechanisms [11].

Interestingly, several variants as well as complex interface structures could be formed as a product of the martensitic bcc → hcp transformation. Many previous studies have been devoted to the intriguing microstructure of the transformation products in Ti-based materials [4,16,17]. For example, Banerjee et al. [17] analyzed the formation of complex substructures in the hcp martensite formed from the quenching of the high-temperature bcc Ti alloy. They proposed the mechanism that the martensitic domains nucleate and propagate until reaching each other and form stacking antiphase boundaries with a displacement vector of either $1/3\langle 10\bar{1}0\rangle$ or $1/6\langle 20\bar{2}3\rangle$. Matsuda et al. [16] used transmission electron microscopy to investigate the formation of antiphase boundary-like structures in the B19 martensite of Ti-Pd alloy, which is induced by the local heterogeneity of atomic movements during the B2 to B19 martensitic transformation. Recently, more numerical simulations and theoretical calculations have been conducted, which provided even further understanding of the transformation product [18–22]. For instance, Gao et al. [18] used molecular dynamics (MD) simulations to investigate the diffuse scattering pattern prior to the bcc-hcp martensitic transformation, which was ascribed to the formation of pairs of hcp anti-variants. In another study, Shi et al. [20] developed a 3D phase-field model to investigate the influence of both external and internal stress on

* Corresponding author.
E-mail address: leicao@unr.edu (L. Cao).
[1] Both authors contributed equally to this work.

https://doi.org/10.1016/j.actamat.2022.118377
1359-6454/

the variant selection during precipitation in Ti-6Al-4V alloy. They found that uniaxial tensile and compressive stress along $[010]_{bcc}$-axis lead to the selection of 8 and 4 out of the 12 hcp variants, respectively. Furthermore, Wang et al. [19] calculated the shape strains created by martensitic bcc → hcp transformation in pure Ti. They found that clusters of three hcp variants could achieve the greatest degree of self-accommodation, in which three slip systems provide complementary shear.

Besides domain boundaries, twin boundaries are another prevalent interface formed during the martensitic bcc-hcp transformation. In the theories of martensite crystallography, besides lattice change, an additional deformation that often induces twinning is an indispensable component to complete the phase transformation. These theories have been successfully applied to predict and explain the macroscopic features of phase transformation, such as experimentally observed habit planes. It should also be noted that there exists a different interpretation on twinning in martensitic phase transformation. In particular, twinning does not form due to the additional deformation accompanying the lattice change, but the two twinned product phases form directly from the parent phase by means of crystallographically equivalent correspondences [23,24]. Along this view, the terminology of transformation twin is suggested, and fruitful new insights have been obtained lately [25–30]. For example, both $\{10\bar{1}1\}$ and $\{10\bar{1}2\}$ twins were reported as transformation twins in pure Ti and its alloys [23,31–33]. Furthermore, Gao et al. [29] utilized these transformation twins formed during cyclic bcc-hcp-bcc phase transformation to design multigrain structures. Under uniaxial compression, the single-crystal bcc transformed into two hcp variants with the $\{10\bar{1}2\}$ twin formed in between. Subsequently, the reheating process to the bcc-stable regime produced more inclined transformation twins and yielded multigrain structures [29]. Additionally, the cyclic hcp-bcc-hcp transition pathway is infinite because the two phases do not have a group-subgroup relation. As a result, all the twinning modes in hcp metals were successfully derived based on certain reversible phase transformations [30]. In the MD simulation by Chen et al. [28], they observed that a reversible hcp-bcc-hcp transformation leads to the formation of $\{10\bar{1}2\}$ twins in Ti. In our previous MD simulations of ω-Ti (the high pressure phase for Ti with AlB2 structure), we found that stress-induced ω to hcp martensitic transformation can produce four types of transformation twins, namely, $\{10\bar{1}2\}$, $\{10\bar{1}1\}$, $\{11\bar{2}2\}$, and $\{11\bar{2}1\}$ twins, each formed under different loading directions [27]. This new knowledge of transformation twins can guide the experimental characterization of the complicated and dense microstructure of shock/pressure recovered ω/hcp structures. In this study, we take a step further to investigate the role of the mechanical loading in the activation of different phase transformation mechanisms, and accordingly the formation of different transformation twins. We discover tension/compression asymmetry in the transformation twins, which is determined by the correlation between the loading direction and the transformation strain. Furthermore, our MD simulations and theoretical calculations allow us to uniquely determine the twinning components of each transformation twin.

This paper is organized as follows. Section 2 describes the methods for the atomistic simulations. Section 3 shows the MD simulations in polycrystal Ti, the strain calculation for the tension/compression asymmetry, and the twinning mode analysis for each twin observed. Finally, we present the conclusions in Section 4.

2. Methods

In the current study, the LAMMPS package [34] is used to conduct the molecular dynamics (MD) simulations. The initial structure ($29.5 \times 25.5 \times 24.1$ nm^3) contains one million Ti atoms

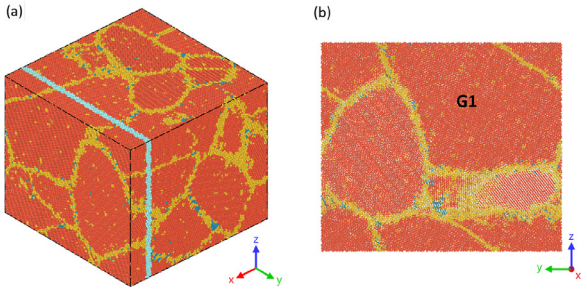

Fig. 1. (a) The simulation domain is a polycrystal bcc-Ti obtained from melt-quench simulations. The light blue region in (a) corresponds to a thin slice of the simulation domain and is shown in (b). The largest grain in the polycrystal is marked as G1. (For interpretation of the references to color in this figure legend, the reader is referred to the web version of this article.)

Table 1
The comparison between the lattice constants obtained from the experiments [42] and the simulation [35].

	a_{bcc} (A°)	a_{hcp} (A°)	c/a
Experiment	3.26	2.951	1.587
Simulation	3.251	2.947	1.597
Difference	0.27%	0.13%	−0.63%

with periodic boundary conditions applied to all three dimensions. The embedded-atom method potential developed by Mendelev et al. [35] is utilized to model the interactions between Ti atoms. The time-step size of the MD simulations is 1 fs. Initially, the atoms are assigned with random velocities following the Gaussian distribution, corresponding to an average temperature of 10 K. During the melting process, the Ti structure is heated up to 2266 K, which is higher than the melting point of 1923 K, to ensure the complete melting. Then the structure is maintained at 2266 K for 500 ps and subsequently quenched to 10 K. The quenching process produces a metastable bcc-Ti polycrystal (Fig. 1) that is stabilized by the fast quenching rate and the abundant grain boundaries and twin boundaries. Afterwards, the structure is relaxed at 10 K and 0 Pa in the isothermal-isobaric ensemble using the Nose-Hoover thermostat [36] and the Parrinello–Rahman barostat [37] for 100 ps. For the deformation process, the uniaxial loading is applied to the relaxed bcc-Ti polycrystal at a constant temperature of 600 K, unless otherwise stated. Theoretically, a high temperature close to the phase boundary is ideal to observe the bcc-hcp phase transition. In this work, a lower temperature of 600 K is chosen to avoid thermal fluctuation that undermines clear visualization of the microstructure evolution. A similar strategy was adopted in previous MD simulations [38]. In addition, extensive simulations with various strain rates have been conducted in the range of 10^8 s^{-1} to 10^9 s^{-1}. Indeed, the results are found to be strain-rate independent. Finally, OVITO [39] and the common neighbor analysis [40,41] are used to identify the crystal structure, with bcc, hcp, face-centered cubic (fcc), and amorphous phases denoted in red, cyan, green, and yellow, respectively.

The ratio of bcc and hcp lattice parameters is important for strain accommodation. Therefore, the lattice parameters from the simulation [35] and experiments [42] are compared in Table 2. It can be seen that the differences are not significant ($< 1\%$). Therefore, we believe the strain accommodation during the phase transition in the MD simulation is close to the experimental conditions.

3. Results

The initial polycrystal is in the metastable bcc phase. With increasing strain, the metastable bcc phase transforms into the stable

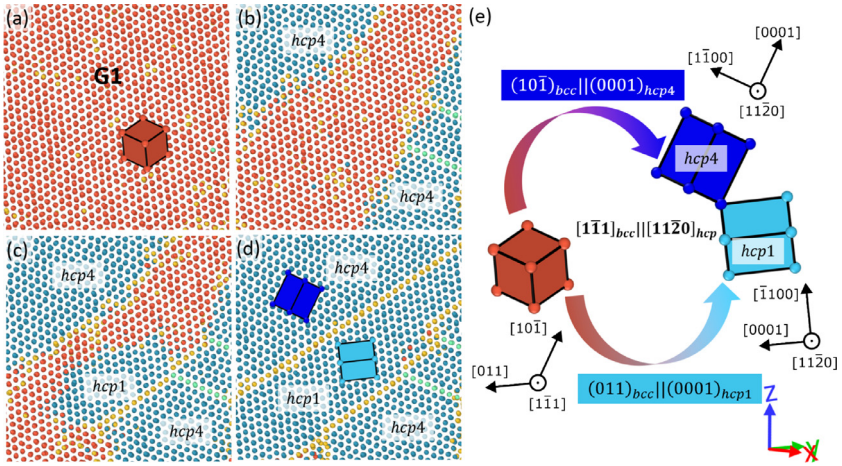

Fig. 2. The formation process of $\{10\bar{1}1\}$ twins during bcc-hcp phase transition under *x*-tension. (a) The grain G1 initially exists in bcc phase. (b) The nucleation of the first variant hcp4 in the top left and bottom right regions of grain G1 at the strain of 5.68%. (c) The nucleation of the second variant hcp1 at the strain of 6.2%. (d) The formation of $\{10\bar{1}1\}$ twins between hcp4 and hcp1 at the strain of 8.4%. (e) A schematic illustrating the orientation relation of the bcc-hcp phase transformation.

hcp phase, forming various martensite microstructure with internal twins. Interestingly, the types of internal twins depend on the loading direction, which is most obvious in the largest grain G1 in the polycrystal (Fig. 1(b)). Therefore, the microstructure evolution in grain G1 will be shown first, followed by the loading direction effect on the twin formation, and finally the analysis of the twinning modes.

We label the six hcp variants according to which bcc plane their basal plane originates from. In this sense, the basal planes of variants hcp1∼hcp6 originate from the bcc planes (011), $(0\bar{1}1)$, (101), $(10\bar{1})$, (110), and $(\bar{1}10)$, respectively. Each pair of hcp variants, hcp1/hcp2, hcp3/hcp4, and hcp5/hcp6 present mirror symmetry. Moreover, a three fold symmetry also exists between the hcp variants. For example, hcp5/hcp1/hcp4 shows a three-fold symmetry around $[1\bar{1}1]_{bcc}$ axis, and hcp5/hcp2/hcp3 shows a three-fold symmetry around $[11\bar{1}]_{bcc}$ axis.

3.1. Molecular dynamics simulations

3.1.1. The formation of $\{10\bar{1}1\}$ twin

Fig. 2 shows the microstructure evolution in grain G1 under *x*-axis tension. As shown in Fig. 2(b), the phase transition initiates simultaneously from the top left and bottom right regions of grain G1, both forming the same hcp phase (hcp4). At a strain of 6.2%, a different hcp phase (hcp1) forms in the middle of grain G1 and is sandwiched between the two regions of previously formed hcp4 (Fig. 2(c)). In particular, the two newly formed hcp phases—hcp4 and hcp1—are misorientated by 57° around a common $\langle 11\bar{2}0\rangle_{hcp}$ axis, which corresponds to a $\{10\bar{1}1\}$ twin relation in hcp materials. Later, two $\{10\bar{1}1\}$ twin boundaries indeed are formed in between hcp4 and hcp1 (Fig. 2(d)).

Furthermore, the crystallography of the above phase transition and twin formation process is examined. Theoretically, the bcc-hcp phase transition can form twelve hcp variants, while grain G1 forms two hcp variants under *x*-tension. Specifically, the basal planes of hcp4 and hcp1 originate from $(10\bar{1})_{bcc}$ and $(011)_{bcc}$ planes in grain G1 that share a common $[1\bar{1}1]_{bcc}$ axis, as illustrated in Fig. 2(e). Therefore, the phase transition follows the Burgers mechanism, $\{110\}_{bcc} \parallel \{0001\}_{hcp}$ and $[1\bar{1}1]_{bcc} \parallel [11\bar{2}0]_{hcp}$ [9]. The orientation relation in each hcp variant is summarized in Eq. (1).

$$\begin{aligned} &bcc \rightarrow hcp4 : (10\bar{1})_{bcc} \parallel (0001)_{hcp4}, [1\bar{1}1]_{bcc} \parallel [11\bar{2}0]_{hcp4} \\ &bcc \rightarrow hcp1 : (011)_{bcc} \parallel (0001)_{hcp1}, [1\bar{1}1]_{bcc} \parallel [11\bar{2}0]_{hcp1} \end{aligned} \quad (1)$$

3.1.2. The formation of $\{10\bar{1}2\}$ twin

We find that the twinning mode changes when changing the loading from *x*-tension to *x*-compression. Fig. 3 shows the microstructure evolution in grain G1 under *x*-compression. The phase transition forms one hcp phase (hcp6) at 5.8% strain (Fig. 3(b)). When the strain reaches 8%, the left region of grain G1 transforms into another hcp phase (hcp5) (Fig. 3(c)). At 11.6% strain, hcp5 and hcp6 meet each other and form a $\{10\bar{1}2\}$ twin, which is characterized by a 86° misorientation across the $\langle 11\bar{2}0\rangle$ zone axis (Fig. 3(d)).

The orientation relation of the above phase transition and twin formation process is further examined. Specifically, the basal planes of hcp5 and hcp6 originate from $(110)_{bcc}$ and $(1\bar{1}0)_{bcc}$ planes in grain G1 that share a common $[001]_{bcc}$ axis, as schematically illustrated in Fig. 3(e). In other words, the bcc-hcp phase transition under *x*-tension follows the Pitsch–Schrader (PS) orientation relation, $\{110\}_{bcc} \parallel (0001)_{hcp}$ and $[001]_{bcc} \parallel [2\bar{1}\bar{1}0]_{hcp}$. The orientation relation in each hcp variant is shown in Eq. (2).

$$\begin{aligned} &bcc \rightarrow hcp6 : \ (1\bar{1}0)_{bcc} \| (0001)_{hcp6}, \quad [001]_{bcc} \| [2\bar{1}\bar{1}0]_{hcp6} \\ &bcc \rightarrow hcp5 : \ (110)_{bcc} \| (0001)_{hcp5}, \quad [001]_{bcc} \| [2\bar{1}\bar{1}0]_{hcp5} \end{aligned} \quad (2)$$

3.1.3. The formation of $\{11\bar{2}2\}$ twin

In the previous two sections, we focused on the largest grain G1 in the bcc polycrystal. It should be noted that the polycrystal also contains $\{112\}_{bcc}$ twins that were formed during the quenching process. The effect of these initial twins on the phase transformation will be investigated next. As shown in Fig. 4(a), the two bcc regions forming the initial $\{112\}_{bcc}$ twin are labelled bcc1 and bcc2. Under *x*-axis tension, the bcc phases start to undergo martensitic phase transformation at 6.04% strain (Fig. 4(b)). The bcc1 and bcc2 transform completely into hcp phases at 7.2% strain (Fig. 4(c)) and 10.24% strain (Fig. 4(d)), respectively. Fig. 4(e) schematically shows the phase transformation in the zone axis of $[011]_{bcc} \parallel [10\bar{1}0]_{hcp}$. Notably, the bcc-hcp phase transformation converts the initial $\{112\}_{bcc}$ twin into a $\{11\bar{2}2\}_{hcp}$ twin. In addition, it should be noted that the misorientation angle of $\{112\}_{bcc}$ twin (70° across $[011]_{bcc}$) is close to that of the $\{11\bar{2}2\}_{hcp}$ twin (65° across $[10\bar{1}0]_{hcp}$), rendering the above twin transformation feasible.

3.1.4. The formation of $\{11\bar{2}1\}$ twin

Interestingly, the same initial $\{112\}_{bcc}$ twin will be converted to different hcp twins depending on the loading direction. Fig. 5 shows the microstructure evolution in the $\{112\}_{bcc}$ twinned

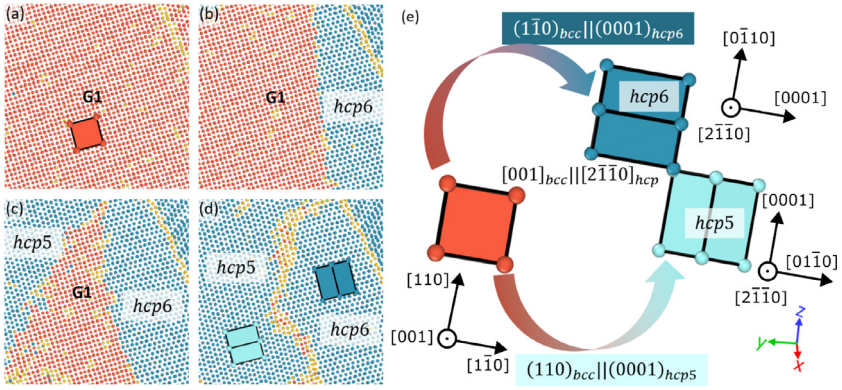

Fig. 3. The formation process of a $\{10\bar{1}2\}$ twin during the bcc-hcp phase transition under *x*-compression. (a) The same grain G1 as in Fig. 2. The formation of (b) the first hcp phase (hcp6) and (c) another hcp variant (hcp5). (d) The growth of two hcp variants leads to the formation of an incoherent $\{10\bar{1}2\}$ twin. (e) A schematic illustrating the orientation relation of the bcc-hcp phase transformation.

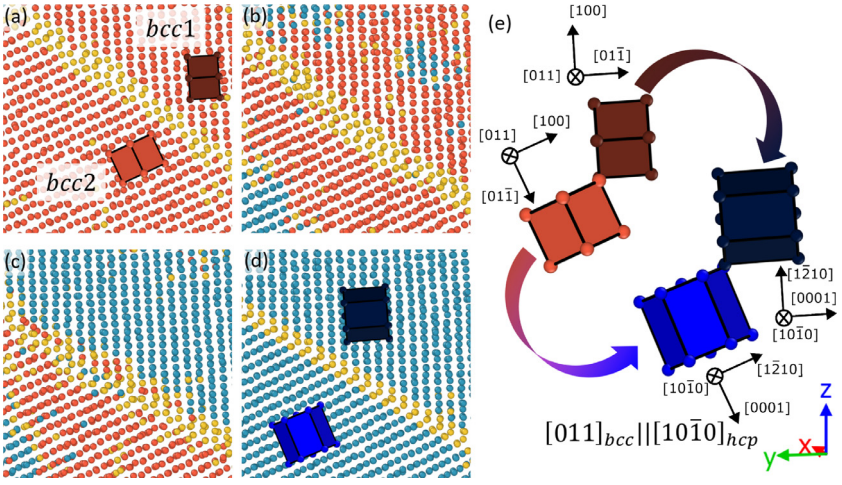

Fig. 4. The bcc-hcp phase transformation converts a $\{112\}_{bcc}$ twin into a $\{11\bar{2}2\}_{hcp}$ twin under *x*-tension. (a) The initial bcc grain contains a $\{112\}_{bcc}$ twin. (b) The nucleation of two hcp variants at the strain of 6.04%. (c) The growing hcp phase consumes bcc1. (d) The second hcp variant consumes bcc2, forming a coherent $\{11\bar{2}2\}_{hcp}$ twin boundary. (e) A schematic illustrating the orientation relation of the bcc-hcp phase transformation.

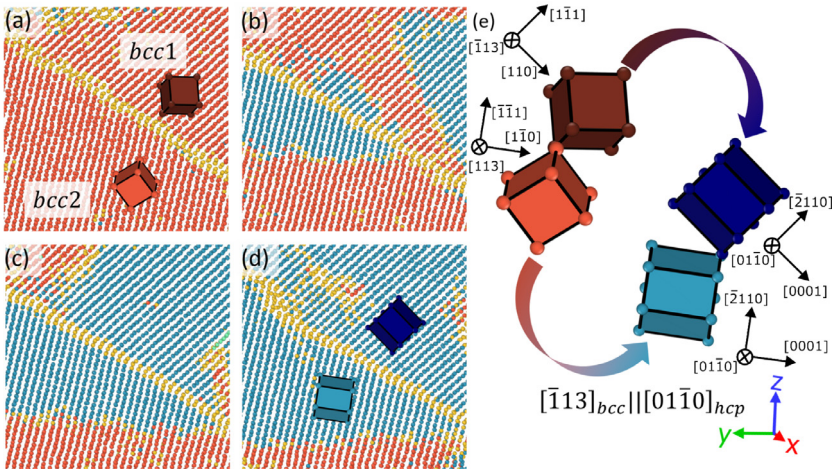

Fig. 5. The bcc-hcp phase transformation converts a $\{112\}_{bcc}$ twin into a $\{11\bar{2}1\}_{hcp}$ twin under *x*-compression. (a) The grain contains a $\{112\}_{bcc}$ twin between bcc1 and bcc2. (b) The formation of the hcp phases at 4.4% strain. (c-d) The growth of the two newly formed hcp phases and the formation of the $\{11\bar{2}1\}_{hcp}$ twin. (e) A schematic illustrating the orientation relation of the bcc-hcp phase transformation.

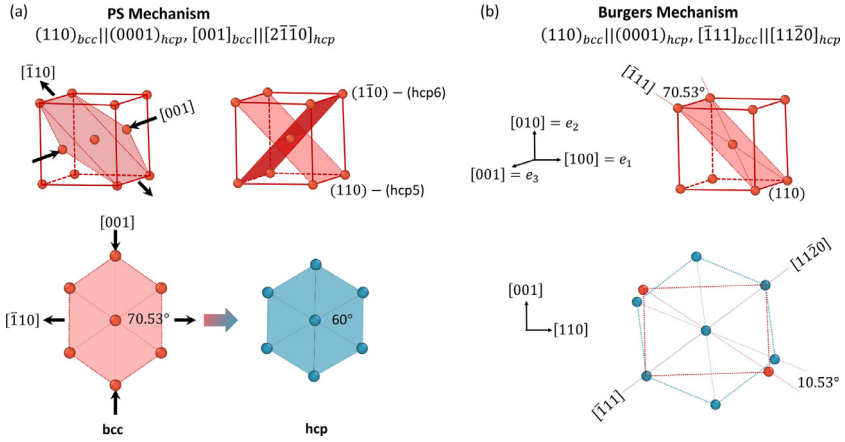

Fig. 6. The orientation of the Cartesian coordinate basis $\mathbf{e}_i$ and the reference bcc lattice. (a) PS mechanism: the top row shows one (110) plane and one $(1\bar{1}0)$ plane involved in the $\{10\bar{1}2\}_{hcp}$ twin case; the bottom row shows the comparison between bcc (110) plane and hcp basal plane in PS mechanism. (b) Burger mechanism: the top row shows one (110) plane in bcc unit cell and the bottom row shows the comparison between bcc (110) plane and hcp basal phase in Burgers mechanism.

grain under x-axis compression. The same labeling rule of bcc1 and bcc2 are adopted in Fig. 5(a) because this is the same grain as in the previous case of x-tension. At 4.4% strain, a new hcp phase nucleates inside bcc1. When the strain reaches 5.12%, another hcp variant nucleates inside bcc2 near the initial $\{112\}_{bcc}$ twin boundary (Fig. 5(b)). Both hcp variants keep growing with increasing strain (Fig. 5(c)). Finally, the original $\{112\}_{bcc}$ twin transforms into a $\{11\bar{2}1\}_{hcp}$ twin, as shown in Fig. 5(d). The phase transitions follow the plane correspondence of $\{110\}_{bcc} \parallel \{0001\}_{hcp}$ and the direction correspondence of $[\bar{1}13]_{bcc} \parallel [01\bar{1}0]_{hcp}$. This process is feasible since the angle between the two $\{110\}_{bcc}$ planes (35° across $[\bar{1}13]_{bcc}$ axis) is close to the misorientation angle (35° across $[01\bar{1}0]_{hcp}$) of $\{11\bar{2}1\}_{hcp}$ twin in hcp materials.

3.2. The effect of the loading direction on the twin formation

In hcp metals, $\{10\bar{1}1\}_{hcp}$ twin is known as compression twin and $\{10\bar{1}2\}_{hcp}$ twin is known as tension twin. Specifically, $\{10\bar{1}1\}_{hcp}$ twin forms when the c-axis is under compression; $\{10\bar{1}2\}_{hcp}$ twin forms when the c-axis is under tension. It is interesting to note similar directional dependence in our MD simulations: the obtained internal twins change from $\{10\bar{1}1\}_{hcp}$ to $\{10\bar{1}2\}_{hcp}$ twins when the loading direction changes from x-tension to x-compression. However, it may not be appropriate to apply the directional dependence in hcp materials directly to rationalize our observation, because the loading in this work is applied to the bcc polycrystal. In this section, we will calculate the deformation gradient associated with the phase transformation to understand the directional dependence observed in our MD simulations.

3.2.1. Unit cell kinematics of bcc → hcp transformation

To understand the impact of loading on the hcp variants and the twins formed in the bcc-hcp phase transition shown in the MD simulations, we make use of the deformation gradient $\mathbf{F}$ associated with the unit cell kinematics throughout this transformation. We start by calculating $\mathbf{F}$ for the PS mechanism, and then derive $\mathbf{F}$ for the Burgers mechanism, since both mechanisms are observed in our simulations.

As shown in Fig. 6, we define a standard rectangular Cartesian coordinate basis aligned with the reference bcc lattice, so that $\mathbf{e}_i$ is an orthonormal basis, $i = \{1, 2, 3\}$, in the [100], [010] and [001] directions, respectively. We further define $\mathbf{v}_1 = (\mathbf{e}_1 - \mathbf{e}_2)/\sqrt{2}$ and $\mathbf{v}_2 = (\mathbf{e}_1 + \mathbf{e}_2)/\sqrt{2}$, pointing respectively in the $[\bar{1}10]$ and [110] directions. A referential bcc orthogonal basis is then $\mathbf{G}_1 = \sqrt{2}\,a_0\,\mathbf{v}_1$, $\mathbf{G}_2 = \sqrt{2}\,a_0\,\mathbf{v}_2$, and $\mathbf{G}_3 = a_0\,\mathbf{e}_3$, where $a_0 = 3.31$ Å is the bcc-Ti lattice parameter. The reciprocal basis $\mathbf{G}^i$ is defined by the relation $\mathbf{G}_i \cdot \mathbf{G}^j = \delta_i^j$, where δ_i^j is a Kronecker delta.

Under PS mechanism (Fig. 6(a)), choosing the particular hcp5 variant with a basal plane originating from $(110)_{bcc}$ plane, the transformation induces the following deformed basis: $\mathbf{g}_1 = \sqrt{3}a\,\mathbf{v}_1$, $\mathbf{g}_2 = c\,\mathbf{v}_2$, and $\mathbf{g}_3 = a\,\mathbf{e}_3$, where $a = 2.95$ Å and $c = 4.68$ Å are the hcp-Ti lattice parameters. The deformed basis $\mathbf{g}_i$ for different hcp variants can be similarly calculated; for example, $\mathbf{g}_1 = c\,\mathbf{v}_1$, $\mathbf{g}_2 = \sqrt{3}a\,\mathbf{v}_2$, and $\mathbf{g}_3 = a\,\mathbf{e}_3$ for the hcp6 variant, whose basal plane originates from the $(1\bar{1}0)_{bcc}$ plane. This allows us to calculate the deformation gradient $\mathbf{F} = \mathbf{g}_i \otimes \mathbf{G}^i$ for a specific variant of the bcc-hcp transformation. Eq. (3) lists the components in matrix form F_{ij} for all the six bcc → hcp transformations, in the standard basis.

$$
\begin{aligned}
F_{ij}|^{PS}_{hcp1} &= \frac{1}{2}\begin{bmatrix} \frac{2a}{a_0} & 0 & 0 \\ 0 & \frac{a}{a_0}\sqrt{\frac{3}{2}} + \frac{c}{\sqrt{2}a_0} & -\frac{a}{a_0}\sqrt{\frac{3}{2}} + \frac{c}{\sqrt{2}a_0} \\ 0 & -\frac{a}{a_0}\sqrt{\frac{3}{2}} + \frac{c}{\sqrt{2}a_0} & \frac{a}{a_0}\sqrt{\frac{3}{2}} + \frac{c}{\sqrt{2}a_0} \end{bmatrix}, \\
F_{ij}|^{PS}_{hcp2} &= \frac{1}{2}\begin{bmatrix} \frac{2a}{a_0} & 0 & 0 \\ 0 & \frac{a}{a_0}\sqrt{\frac{3}{2}} + \frac{c}{\sqrt{2}a_0} & \frac{a}{a_0}\sqrt{\frac{3}{2}} - \frac{c}{\sqrt{2}a_0} \\ 0 & \frac{a}{a_0}\sqrt{\frac{3}{2}} - \frac{c}{\sqrt{2}a_0} & \frac{a}{a_0}\sqrt{\frac{3}{2}} + \frac{c}{\sqrt{2}a_0} \end{bmatrix}, \\
F_{ij}|^{PS}_{hcp3} &= \frac{1}{2}\begin{bmatrix} \frac{a}{a_0}\sqrt{\frac{3}{2}} + \frac{c}{\sqrt{2}a_0} & 0 & -\frac{a}{a_0}\sqrt{\frac{3}{2}} + \frac{c}{\sqrt{2}a_0} \\ 0 & \frac{2a}{a_0} & 0 \\ -\frac{a}{a_0}\sqrt{\frac{3}{2}} + \frac{c}{\sqrt{2}a_0} & 0 & \frac{a}{a_0}\sqrt{\frac{3}{2}} + \frac{c}{\sqrt{2}a_0} \end{bmatrix}, \\
F_{ij}|^{PS}_{hcp4} &= \frac{1}{2}\begin{bmatrix} \frac{a}{a_0}\sqrt{\frac{3}{2}} + \frac{c}{\sqrt{2}a_0} & 0 & \frac{a}{a_0}\sqrt{\frac{3}{2}} - \frac{c}{\sqrt{2}a_0} \\ 0 & \frac{2a}{a_0} & 0 \\ \frac{a}{a_0}\sqrt{\frac{3}{2}} - \frac{c}{\sqrt{2}a_0} & 0 & \frac{a}{a_0}\sqrt{\frac{3}{2}} + \frac{c}{\sqrt{2}a_0} \end{bmatrix}, \\
F_{ij}|^{PS}_{hcp5} &= \frac{1}{2}\begin{bmatrix} \frac{a}{a_0}\sqrt{\frac{3}{2}} + \frac{c}{\sqrt{2}a_0} & -\frac{a}{a_0}\sqrt{\frac{3}{2}} + \frac{c}{\sqrt{2}a_0} & 0 \\ -\frac{a}{a_0}\sqrt{\frac{3}{2}} + \frac{c}{\sqrt{2}a_0} & \frac{a}{a_0}\sqrt{\frac{3}{2}} + \frac{c}{\sqrt{2}a_0} & 0 \\ 0 & 0 & \frac{2a}{a_0} \end{bmatrix}, \\
F_{ij}|^{PS}_{hcp6} &= \frac{1}{2}\begin{bmatrix} \frac{a}{a_0}\sqrt{\frac{3}{2}} + \frac{c}{\sqrt{2}a_0} & \frac{a}{a_0}\sqrt{\frac{3}{2}} - \frac{c}{\sqrt{2}a_0} & 0 \\ \frac{a}{a_0}\sqrt{\frac{3}{2}} - \frac{c}{\sqrt{2}a_0} & \frac{a}{a_0}\sqrt{\frac{3}{2}} + \frac{c}{\sqrt{2}a_0} & 0 \\ 0 & 0 & \frac{2a}{a_0} \end{bmatrix}.
\end{aligned}
\tag{3}
$$

Since the deformation gradient associated with the bcc → hcp transformation only changes by a rotation between the PS and Burgers mechanisms, typically only the right stretch tensor associated with Burgers is discussed [1,43], which is the same for

both deformation paths. However, it is important to keep track of rotations with respect to load directions, since they change $\mathbf{F}$ and can have an impact on certain (non-referential) measures of strain. For the Burgers mechanism (Fig. 6(b)), one diagonal of the $\{110\}_{bcc}$ plane, which transforms into $(0001)_{hcp}$, rotates by $\theta = 10.53^{\circ}$, which is accompanied by lattice stretching. For example, the present basis for hcp5 is $\mathbf{g}_1 = \sqrt{3}a(\cos\theta\,\mathbf{v}_1 - \sin\theta\,\mathbf{e}_3)$, $\mathbf{g}_2 = c\,\mathbf{v}_2$, and $\mathbf{g}_3 = a(\sin\theta\,\mathbf{v}_1 + \cos\theta\,\mathbf{e}_3)$. As a comparison, the components F_{ij} of the deformation gradient for hcp5 and hcp6 under the Burgers mechanism in standard basis are listed in Eq. (4), which presents additional terms as a function of θ when compared to Eq. (3). Note that $\mathbf{F}$ is no longer symmetric for the Burgers mechanism since rotations are present, $\mathbf{Q} \neq \mathbf{I}$.

$$F_{ij}|^{Burgers}_{hcp5} = \frac{1}{2}\begin{bmatrix} \frac{a\cos\theta}{a_0}\sqrt{\frac{3}{2}} + \frac{c}{\sqrt{2}a_0} & -\frac{a\cos\theta}{a_0}\sqrt{\frac{3}{2}} + \frac{c}{\sqrt{2}a_0} & \frac{2a\sin\theta}{\sqrt{2}a_0} \\ -\frac{a\cos\theta}{a_0}\sqrt{\frac{3}{2}} + \frac{c}{\sqrt{2}a_0} & \frac{a\cos\theta}{a_0}\sqrt{\frac{3}{2}} + \frac{c}{\sqrt{2}a_0} & -\frac{2a\sin\theta}{\sqrt{2}a_0} \\ -\frac{a\sqrt{3}\sin\theta}{a_0} & \frac{a\sqrt{3}\sin\theta}{a_0} & \frac{2a}{a_0} \end{bmatrix}, \tag{4}$$

$$F_{ij}|^{Burgers}_{hcp6} = \frac{1}{2}\begin{bmatrix} \frac{a\cos\theta}{a_0}\sqrt{\frac{3}{2}} + \frac{c}{\sqrt{2}a_0} & \frac{a\cos\theta}{a_0}\sqrt{\frac{3}{2}} - \frac{c}{\sqrt{2}a_0} & -\frac{2a\sin\theta}{\sqrt{2}a_0} \\ \frac{a\cos\theta}{a_0}\sqrt{\frac{3}{2}} - \frac{c}{\sqrt{2}a_0} & \frac{a\cos\theta}{a_0}\sqrt{\frac{3}{2}} + \frac{c}{\sqrt{2}a_0} & -\frac{2a\sin\theta}{\sqrt{2}a_0} \\ \frac{a\sqrt{3}\sin\theta}{a_0} & \frac{a\sqrt{3}\sin\theta}{a_0} & \frac{2a}{a_0} \end{bmatrix}.$$

3.2.2. X-*tension:* $\{10\bar{1}1\}$ *twin*

After calculating the deformation gradient, we can further compare the strain associated with the phase transformation with the applied loading, to examine the directional dependence observed in our MD simulations. By the polar decomposition, the deformation gradient can be decomposed as $\mathbf{F} = \mathbf{Q}\cdot\mathbf{U} = \mathbf{V}\cdot\mathbf{Q}$, where $\mathbf{U}$ and $\mathbf{V}$ are symmetric positive definite stretch tensors, and $\mathbf{Q}$ is an orthogonal tensor, which allows us to define the Biot strain [44] $\mathbf{E}_{\text{Biot}} = \mathbf{U} - \mathbf{I}$. Other measures of strain include the Bell strain $\mathbf{E}_{\text{Bell}} = \mathbf{V} - \mathbf{I}$, and, for small deformations, the small strain tensor $\boldsymbol{\epsilon} = (1/2)(\mathbf{F} + \mathbf{F}^{\top} - 2\mathbf{I})$. For the bcc to hcp $\mathbf{F}$ based on the PS mechanism, $\mathbf{Q}$ is the identity (no rotation) and $\mathbf{F} = \mathbf{U} = \mathbf{V}$. The right stretch $\mathbf{U}$ for the Burgers mechanism coincides with the one from PS, but since rotations are present for Burgers, both $\mathbf{F}$ and the left stretch $\mathbf{V}$ change. Now, define $\mathbf{d}$ as the unit vector in the load direction. When the strain $e_d = (\mathbf{E}_{\text{Biot}}\cdot\mathbf{d})\cdot\mathbf{d} > 0$ for a specific variant, we say the transformation is kinematically preferred by tension in the $\mathbf{d}$ direction accordingly to the Biot measure, and by compression in the opposite case $e_d < 0$.

In the x-tension case (Fig. 2) starting from a single bcc grain, the tensile load is approximately aligned with $[1\bar{1}1]_{bcc}$ axis. Therefore, we set $\mathbf{d}$ as the unit vector in this direction and calculate the strain e_d for the six hcp variants based on $\mathbf{F}$ for the Burgers mechanism Eq. (4). We find that only three hcp variants present positive e_d strains: hcp1, hcp4, and hcp5, with $e_d = 2.48\times10^{-2}$. These variants can combine to form $\{10\bar{1}1\}$ compression twins, which agrees with our observation in Fig. 2. In the MD simulations, hcp4 forms first, followed by hcp1 and twinning, but we did not find the formation of hcp5. A possible reason is that the load direction presents a small deviation with respect to $[1\bar{1}1]_{bcc}$, which introduces bias in the results. While the discussed strain measures coincide for the PS mechanism, it is worth noting that for the Burgers mechanism this analysis does depend on the choice of strain. For example, only hcp1 presents a positive strain in the $[1\bar{1}1]_{bcc}$ direction with respect to the Bell or small strain tensors, whereas for hcp4 and hcp5 strains are negative but small in magnitude compared to the other variants.

After revealing that the loading of x-tension favors the formation of hcp4 and hcp1, we will further examine the crystallographic relation between the two hcp variants. First, the $(10\bar{1})_{bcc}$ and $(011)_{bcc}$ planes—corresponding to the basal planes of hcp4 and hcp1—form an angle of 60°. Since this angle would remain approximately the same during the bcc-hcp phase transition, hcp4 and hcp1 should have a misorientated angle around 60°. Second, the $(10\bar{1})_{bcc}$ and $(011)_{bcc}$ planes share a common $[1\bar{1}1]_{bcc}$ axis, which later transforms into a common $[11\bar{2}0]_{hcp}$ shared between hcp4 and hcp1. In other words, the misorientation angle and common zone axis agree with those for $\{10\bar{1}1\}$ twin. Thus, $\{10\bar{1}1\}$ twin is expected to form between hcp4 and hcp1.

3.2.3. X-*compression:* $\{10\bar{1}2\}$ *twin*

As for the case of x-compression (Fig. 3) starting from a single bcc grain, the reference lattice has its $[001]_{bcc}$ closely aligned with the out of plane x-direction of the compression load. For both hcp5 and hcp6 variants, based on either PS (3) or Burgers (4) mechanism kinematics, $U_{33} = a/a_0 \approx 0.89$ and $e_d = -1.09\times10^{-1}$, so that the referential bcc lattice has to compress in the $\mathbf{d} = [001]_{bcc}$ direction in order to transform in these hcp variants. In contrast, the other four hcp variants present a positive normal Biot strain along $[001]_{bcc}$. Therefore, the loading of x-compression is expected to favor the formation of hcp5 and hcp6 variants. This observation holds regardless of the choice of strain for this particular load direction.

Further examination of the crystallographic relation reveals that $\{10\bar{1}2\}$ twin will form in between hcp5 and hcp6. First, $(110)_{bcc}$ and $(\bar{1}10)_{bcc}$ planes—corresponding to the basal planes of hcp5 and hcp6—form an angle of 90°, which would remain during the bcc-hcp phase transition and hcp5 and hcp6 are approximately misorientated by 90°. Second, the $(110)_{bcc}$ and $(\bar{1}10)_{bcc}$ planes share a common $[001]_{bcc}$, which under the PS mechanism transforms into a common $[11\bar{2}0]_{hcp}$ shared between hcp5 and hcp6. As the misorientation angle and the common zone axis agree with those in $\{10\bar{1}2\}$ twin, $\{10\bar{1}2\}$ twin is expected to form between hcp5 and hcp6, which agrees with our MD simulation shown in Fig. 3.

3.2.4. X-*tension:* $\{11\bar{2}2\}$ *twin*

So far we have evaluated the role of the load on transformations starting from a single bcc grain. When the reference microstructure contains a $\{112\}_{bcc}$ twin, the analysis becomes more intricate since one needs to account for a pre-strained bcc twin. As discussed by Gao et al. [45], when a bcc transforms into a bcc twin through a hcp-related path, there are twelve (non-identity) lattice correspondences leading to distinct deformation gradients $\mathbf{F}_{\{112\}twin}$. For the simulation in Fig. 4, a tensile load is applied in the $[011]_{bcc}$ direction, and the initial $\{112\}_{bcc}$ microstructure transforms into a $\{11\bar{2}2\}_{hcp}$ twin.

From Eq. (3), we find that the only hcp variant favored by a tensile load in the $\mathbf{d}$ direction is hcp2, with $e = 9.15\times10^{-2}$. This corresponds to the transformation undergone by the parent strain-free bcc lattice in Fig. 4, which becomes hcp2 with $\mathbf{F} = \mathbf{F}|^{PS}_{hcp2}$. In this scenario we will assume the PS mechanism a priori, since the right stretch for both mechanisms is the same and this simplifies the analysis. However, the total deformation gradient $\mathbf{F}^*$ of the bcc twin transformation needs to account for the initial $\mathbf{F}_{\{112\}twin}$, so that $\mathbf{F}^* = \mathbf{F}|^{PS}_{hcp2}\cdot\mathbf{F}_{\{112\}twin}$. Since only hcp2 is preferred by the load, we assume a $\{112\}$ bcc twin $\rightarrow$ hcp2 transformation, where $\mathbf{F}_{\{112\}twin}$ has the following components

$$F_{ij}|_{\{112\}twin} = \begin{bmatrix} 0.5 & -0.75 & 0.75 \\ 0.5 & 0.75 & 0.25 \\ -0.5 & 0.25 & 0.75 \end{bmatrix}. \tag{5}$$

This leads to a resulting $\mathbf{F}^*$ with a Biot strain $e^*_d = 9.15\times10^{-2}$, also favored by the tensile load.

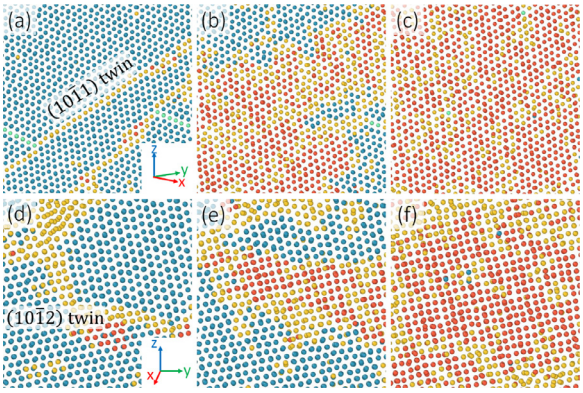

Fig. 7. Transformation of the {10$\bar{1}$1} twin (top row) and {10$\bar{1}$2} twin (bottom row) to single-crystal bcc phase after increasing the temperature from 600 K to 1200 K, confirming that they are the transformation twins associated with bcc → hcp phase transformation.

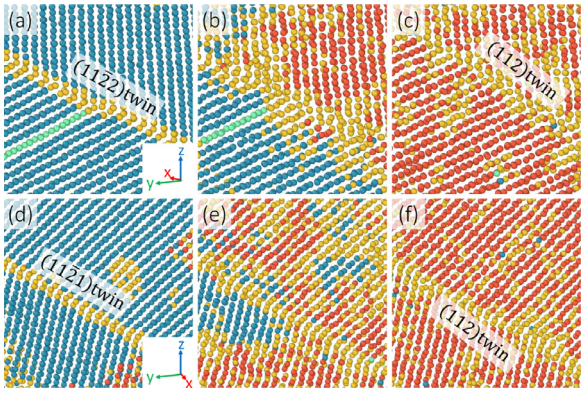

Fig. 8. Transformation of the {11$\bar{2}$2} twin (top row) and {11$\bar{2}$1} twin (bottom row) to $\{112\}_{bcc}$ twin after increasing the temperature from 600 K to 1200 K.

3.2.5. X-*compression:* {11$\bar{2}$1} *twin*

The last case we presented was the {11$\bar{2}$1} twin formation starting from a $\{112\}_{bcc}$ twin. The analysis follows the same steps as in the {11$\bar{2}$2} twin case, where the difference now is that we have a compressive load in the $[\bar{1}13]_{bcc}$ direction. Calculating the Biot strains in this direction based on the deformation gradients from Eq. (3), we find that only hcp5 with $e_d = -7.2 \times 10^{-2}$ and hcp6 with $e_d = -8.9 \times 10^{-2}$ are favored by the compressive load.

The numerical results in Fig. 5 suggest that the parent strain-free bcc lattice transforms into hcp5, with $\mathbf{F} = \mathbf{F}|^{PS}_{hcp5}$, whereas the other lattice forming the twin would come from a different variant. As in the {11$\bar{2}$2} case, this variant originates from a pre-strained bcc twin, with a total deformation gradient $\mathbf{F}^* = \mathbf{F}|^{PS}_{hcp6} \cdot \mathbf{F}_{\{112\}twin}$. Since hcp6 is the other variant preferred by the load, we assume a bcc twin → hcp6 transformation, where $\mathbf{F}_{\{112\}twin}$ components are the same as in Eq. (5). This leads to a resulting $\mathbf{F}^*$ with a Biot strain $e^*_d = -8.1 \times 10^{-2}$ also favored by the compressive load.

3.3. The twinning mode analysis

So far, our MD simulations of bcc → hcp phase transition captured the formation of {10$\bar{1}$1}, {10$\bar{1}$2}, {11$\bar{2}$2} and {11$\bar{2}$1} twins, which are also known as the four deformation twinning modes in hcp materials [46]. It should be noted that both phase transitions and mechanical loadings could lead to twin formation. The former leads to transformation twins and the latter leads to deformation twins [47–49]. The twin components for deformation twins are well-established [46], while that for the transformation twin is still unclear [47–49], especially on the relation between the transformation twins and deformation twins.

3.3.1. Reverse phase transition

To unambiguously determine the transformation twin, we further induce the reverse hcp → bcc transformation by heating up these twinned structures to 1200 K. If the twin is the direct product of bcc → hcp transformation, the reverse hcp → bcc transformation will eliminate the twin boundary and lead to a single bcc phase. Figs. 7 and 8 demonstrate the microstructure evolution of the four types of twins during the heating process. For the {10$\bar{1}$1} twin, only one bcc phase nucleates from the {10$\bar{1}$1} twin boundaries (Fig. 7(b)) and then consumes the entire twinned grain (Fig. 7(c)). Similarly, the same phenomenon occurs in the {10$\bar{1}$2} twinned case (Fig. 7(d)–(f)). In contrast, heating up the {11$\bar{2}$2} twin leads to the nucleation of two different bcc phases and the formation of a {112} twin (Fig. 8(c)), so does the case of the {11$\bar{2}$1} twin (Fig. 8(f)). To conclude, only {10$\bar{1}$1} and {10$\bar{1}$2} twins are transformation twins associated with bcc → hcp phase transformation. The formation of {11$\bar{2}$2} and {11$\bar{2}$1} twins is ascribed to the existing {112} twin in the parent bcc phase, formed before the bcc → hcp phase transformation.

Previously, {10$\bar{1}$1} twins were identified as transformation twins in pure Ti, caused by quenching-induced bcc → hcp phase transformation [23,31,32]. In Ti alloy [33], quenching-induced {10$\bar{1}$2} transformation twins were reported. Our MD simulations agree with the experimental observation of transformation twins in Ti and its alloys. More importantly, our analysis in Section 3.2 reveals that the activation of the specific transformation twinning mode is selected by the applied mechanical loading. This new knowledge could offer a novel strategy for engineering twin microstructure using designed thermomechanical processing [21,22,29]. Finally, it should be noted that this is not specific to Ti and its alloys, and should apply generally to other material systems involving bcc → hcp phase transformation.

3.3.2. Theoretical calculation

Last but not the least, the twinning mode of the transformation twins will be examined to understand its relevance to the deformation twinning modes in hcp metals. In Section 3.2 we were able to identify the deformation gradients associated with the different hcp variants observed in the resulting microstructure. We can now employ these tensors to calculate the twinning elements between each pair of variants, and compare with the MD results. These elements are the solution of the twinning equation [50], a kinematic compatibility condition between two regions presenting a jump in the deformation gradient and stretch. If a twin is formed between variants I and J, with right stretch tensors $\mathbf{U}_I$ and $\mathbf{U}_J$, then the twinning equation takes the form

$$\mathbf{R} \cdot \mathbf{U}_I - \mathbf{U}_J = \mathbf{a} \otimes \mathbf{n}, \tag{6}$$

for some vector $\mathbf{a}$ and a unit normal $\mathbf{n}$ to the interface. The misorientation between the neighboring lattices is captured by the rotation tensor $\mathbf{R}$.

Once the stretch tensors $\mathbf{U}_I$ and $\mathbf{U}_J$ are extracted from the deformation gradients, a pair of solutions $\{\mathbf{a}, \mathbf{n}, \mathbf{R}\}$ can be calculated from (6) based on the algorithm detailed by Bhattacharya [51]. In the present case, $\mathbf{n}$ can be identified with the normal for the shear plane K in the hcp lattice, whereas the direction of shear η and shear magnitude s are calculated as

$$\eta = \frac{\mathbf{a}}{|\mathbf{a}|}, \quad s = |\mathbf{a}|\,|\mathbf{U}_J^{-1} \cdot \mathbf{n}|. \tag{7}$$

Following this approach, we use the deformation gradients predicted in Section 3.2 to calculate the twinning elements for each case.

Table 2
Summary of the twinning modes observed after bcc → hcp phase transformation. * The angles between bcc planes involved in the twin formation process is taken as an acute angle to be consistent with the definition of the misorientation angles of the twins.

Twin type	bcc→ $\{10\bar{1}1\}_{hcp}$	bcc→ $\{10\bar{1}2\}_{hcp}$	$\{112\}_{bcc} \rightarrow \{11\bar{2}2\}_{hcp}$	$\{112\}_{bcc} \rightarrow \{11\bar{2}1\}_{hcp}$
K_2 plane	$\{0.24\ \bar{1}\ 0.76\ \overline{0.28}\}$	$\{\bar{1}012\}$	$\{\bar{1}\bar{1}2\bar{6}\}$	$\{\overline{0.97}\ \overline{0.66}\ 1.62\ \bar{1}\}$
shear s	0.343	0.176	0.152	0.514
loading direction	x-tension	x-compression	x-tension	x-compression
zone axis	$[1\bar{1}1]_{bcc} \parallel [11\bar{2}0]_{hcp}$	$[001]_{bcc} \parallel [2\bar{1}\bar{1}0]_{hcp}$	$[011]_{bcc} \parallel [10\bar{1}0]_{hcp}$	$[\bar{1}13]_{bcc} \parallel [01\bar{1}0]_{hcp}$
bcc-hcp pathway	Burgers	PS	PS	Burgers
bcc planes angle*	60°	90°	70°	35°
twin angle	57°	85°	65°	35°

1. x-tension along $[1\bar{1}1]_{bcc}$: from $\mathbf{F}|^{PS}_{hcp1}$ and $\mathbf{F}|^{PS}_{hcp4}$ we find

   $s = 0.343$,
   $K_1 = \{10\bar{1}\bar{1}\}, \eta_1 = \langle\overline{0.38}\ 1\ \overline{0.62}\ 0.25\rangle$,
   $K_2 = \{0.24\ \bar{1}\ 0.76\ \overline{0.28}\}, \eta_2 = \langle\bar{5}143\rangle$.

2. x-compression along $[001]_{bcc}$: from $\mathbf{F}|^{PS}_{hcp5}$ and $\mathbf{F}|^{PS}_{hcp6}$ we find

   $s = 0.176$,
   $K_1 = \{0\bar{1}12\}, \eta_1 = \langle01\bar{1}1\rangle$,
   $K_2 = \{01\bar{1}2\}, \eta_2 = \langle0\bar{1}11\rangle$.

3. x-tension along $[011]_{bcc}$: from $\mathbf{F}|^{PS}_{hcp2}$ and $\mathbf{F}|^{PS}_{hcp2} \cdot \mathbf{F}_{\{112\}twin}$ we find

   $s = 0.152$,
   $K_1 = \{\bar{1}\bar{1}22\}, \eta_1 = \langle11\bar{2}3\rangle$,
   $K_2 = \{\bar{1}\bar{1}2\bar{6}\}, \eta_2 = \langle11\bar{2}\bar{1}\rangle$.

4. x-compression along $[\bar{1}13]_{bcc}$: from $\mathbf{F}|^{PS}_{hcp5}$ and $\mathbf{F}|^{PS}_{hcp6} \cdot \mathbf{F}_{\{112\}twin}$ we find

   $s = 0.514$,
   $K_1 = \{\bar{1}2\bar{1}\bar{1}\}, \eta_1 = \langle0.83\ 0.17\ \bar{1}\ 0.51\rangle$,
   $K_2 = \{\overline{0.97}\ \overline{0.66}\ 1.62\ \bar{1}\}, \eta_2 = \langle5\bar{7}23\rangle$.

Therefore, based on the deformation gradients and the respective hcp variants favored by the load in each case, we find twinning planes K_1 that exactly match the ones formed in the MD simulations. In particular, the $\{10\bar{1}2\}$ transformation twin is determined to resemble the $\{10\bar{1}2\}$ deformation twinning mode common to all hcp metals. The $\{11\bar{2}2\}$ twin inherited from the $\{112\}_{bcc}$ twin is the same as the $\{11\bar{2}2\}$ extension twin formed through non-cozone $\{10\bar{1}2\}$ – $\{01\bar{1}2\}$ twin-twin interaction [38]. Because these two twinning modes correspond to the deformation twinning modes, their dichromatic complex patterns are shown in Fig. 9. As for the $\{10\bar{1}1\}$ and the $\{11\bar{2}1\}$ twins, the twinning elements calculation clearly demonstrates that they have irrational K_2 planes and η_1 direction, which is different from the well-known $\{10\bar{1}1\}$ and $\{11\bar{2}1\}$ deformation twinning modes. While these solutions for the twinning equation were previously discussed in Gao et al. [30], we here show the effect of mechanical loading. It is possible to predict which twin will be formed by combining the loading analysis for preferred variants with the twinning equation in Eq. (6). Finally, the twinning elements and the corresponding loading condition are summarized in Table 2.

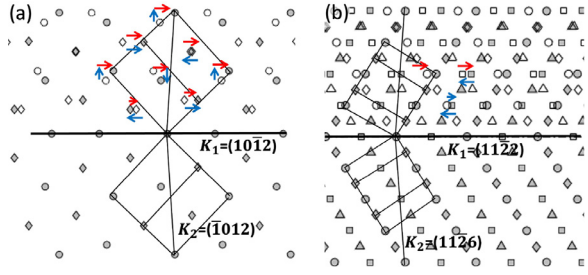

Fig. 9. The dichromatic complex of (a) $\{10\bar{1}2\}$ and (b) $\{11\bar{2}2\}$ twins. The top open symbols and bottom gray symbols represent the parent, while the top gray symbols represent the twin. The blue arrows represent the atomic shuffle direction and the red atoms represent the shear direction. K_1 is the twinning plane and K_2 is the conjugate twinning plane. (For interpretation of the references to color in this figure legend, the reader is referred to the web version of this article.)

4. Conclusions

In conclusion, our MD simulations revealed the formation of martensite microstructure containing $\{10\bar{1}1\}$, $\{10\bar{1}2\}$, $\{11\bar{2}2\}$, and $\{11\bar{2}1\}$ twins as a result of bcc-hcp martensitic phase transformation. Specifically, the $\{10\bar{1}1\}$ and $\{10\bar{1}2\}$ twins are found as the transformation twins, while the $\{11\bar{2}2\}$ and $\{11\bar{2}1\}$ twins are inherited from the initial $\{112\}$ twin in the bcc phase. The twinning mode analysis unambiguously reveals $\{10\bar{1}2\}$ transformation twins correspond to the well-established deformation twinning modes in hcp metals. More importantly, aided by the calculation of the deformation gradient and transformation strain, we explained that the $\{10\bar{1}1\}$ transformation twin is favored by $[1\bar{1}1]_{bcc}$ axis tension and the $\{10\bar{1}2\}$ transformation twin is favored by $[001]_{bcc}$ axis compression. Notably, the calculation completely agrees with our MD simulations, revealing the critical role of mechanical loading on the activation of the specific transformation twinning mode. This new knowledge will offer a novel strategy to engineer twin microstructure using designed thermomechanical processing.

Data availability

The data that support the findings of this study are available from the corresponding author upon reasonable request.

Declaration of Competing Interest

The authors declare that they have no known competing financial interests or personal relationships that could have appeared to influence the work reported in this paper.

Acknowledgments

The authors acknowledge the partial financial support from NSF-CBET TTP-Thermal Transport Process Program and NSF EPSCoR Program (Grant no. #1953300). The authors also would like to acknowledge the support of Research & Innovation and the Office of Information Technology at the University of Nevada, Reno for computing time on the Pronghorn High-Performance Computing Cluster. E.V. is thankful to James Hanna for his support through the NSF grant CMMI-2001262.

References

[1] K.J. Caspersen, A. Lew, M. Ortiz, E.A. Carter, Importance of shear in the bcc–to-hcp transformation in iron, Phys. Rev. Lett. 93 (11) (2004) 115501.
[2] M. Ekman, B. Sadigh, K. Einarsdotter, P. Blaha, Ab initio study of the martensitic bcc-hcp transformation in iron, Phys. Rev. B 58 (9) (1998) 5296.
[3] S. Banerjee, P. Mukhopadhyay, Phase Transformations: Examples from Titanium and Zirconium Alloys, Elsevier, 2010.
[4] K. Otsuka, X. Ren, Physical metallurgy of Ti–Ni-based shape memory alloys, Prog. Mater. Sci. 50 (5) (2005) 511–678.
[5] J.W. Christian, The theory of transformations in metals and alloys, Pergamon, Oxford, 2002, pp. 1–22.
[6] C. Cayron, F. Barcelo, Y. de Carlan, The mechanisms of the fcc bcc martensitic transformation revealed by pole figures, Acta Mater. 58 (4) (2010) 1395–1402.
[7] S.M.C. Van Bohemen, J. Sietsma, S. Van der Zwaag, Experimental observations elucidating the mechanisms of structural bcc-hcp transformations in β Ti alloys, Phys. Rev. B 74 (13) (2006) 134114.
[8] H. Zong, P. He, X. Ding, G.J. Ackland, Nucleation mechanism for hcp bcc phase transformation in shock-compressed Zr, Phys. Rev. B 101 (14) (2020) 144105.
[9] W.G. Burgers, On the process of transition of the cubic-body-centered modification into the hexagonal-close-packed modification of zirconium, Physica 1 (7–12) (1934) 561–586.
[10] K. Masuda-Jindo, S.R. Nishitani, V. Van Hung, Hcp-bcc structural phase transformation of titanium: analytic model calculations, Phys. Rev. B 70 (18) (2004) 184122.
[11] S. Merkel, A. Lincot, S. Petitgirard, Microstructural effects and mechanism of bcc-hcp-bcc transformations in polycrystalline iron, Phys. Rev. B 102 (10) (2020) 104103.
[12] T.H. Lee, H.Y. Ha, J.Y. Kang, J. Moon, C.H. Lee, S.J. Park, An intersecting-shear model for strain-induced martensitic transformation, Acta Mater. 61 (19) (2013) 7399–7410, doi:10.1016/J.ACTAMAT.2013.08.046.
[13] S. Kante, A. Leineweber, Two-phase and three-phase crystallographic relationships in white-solidified and nitrided Fe–C–Si cast iron, Acta Mater. 170 (2019) 240–252, doi:10.1016/J.ACTAMAT.2019.03.029.
[14] J. Ribis, S. Doriot, F. Onimus, Shape, orientation relationships and interface structure of beta-Nb nano-particles in neutron irradiated zirconium alloy, J. Nucl. Mater. 511 (2018) 18–29, doi:10.1016/J.JNUCMAT.2018.08.042.
[15] J.P. Zhou, D.S. Zhao, O. Zheng, J.B. Wang, D.X. Xiong, Z.F. Sun, J.N. Gui, R.H. Wang, High-resolution electron microscopy observations of continuous precipitates with Pitsch–Schrader orientation relationship in an mgal based alloy and interpretation with the O-lattice theory, Micron 40 (8) (2009) 906–910, doi:10.1016/J.MICRON.2009.05.008.
[16] M. Matsuda, T. Hara, M. Nishida, Crystallography and morphology of antiphase boundary-like structure induced by martensitic transformation in Ti–Pd shape memory alloy, Mater. Trans. 49 (3) (2008) 461–465.
[17] D. Banerjee, K. Muraleedharan, J. Strudel, Substructure in titanium alloy martensite, Philos. Mag. A 77 (2) (1998) 299–323.
[18] L. Gao, X. Ding, H. Zong, T. Lookman, J. Sun, X. Ren, A. Saxena, Diffuse scattering as an indicator for martensitic variant selection, Acta Mater. 66 (2014) 69–78.
[19] S. Wang, M. Aindow, M. Starink, Effect of self-accommodation on α/α boundary populations in pure titanium, Acta Mater. 51 (9) (2003) 2485–2503.
[20] R. Shi, Y. Wang, Variant selection during α precipitation in Ti–6Al–4V under the influence of local stress—A simulation study, Acta Mater. 61 (16) (2013) 6006–6024.
[21] C. Jourdan, J. Gastaldi, P. Marzo, G. Grange, In situ statistical study of the nucleation, the variant selection and the orientation memory effect during the $\alpha\beta$ titanium martensitic transformation, J. Mater. Sci. 26 (16) (1991) 4355–4360.
[22] I. Lonardelli, N. Gey, H.-R. Wenk, M. Humbert, S. Vogel, L. Lutterotti, In situ observation of texture evolution during $\alpha\beta$ and $\beta\alpha$ phase transformations in titanium alloys investigated by neutron diffraction, Acta Mater. 55 (17) (2007) 5718–5727.
[23] E. Bilby, The mechanism of phase transformations in metals: martensitic transformations, in: A Symposium Organized by the Institute of Metals and Held at the Royal Institution, London, on 9 Nov. 1955, vol. 18, 1955, p. 121.
[24] B.A. Bilby, J. Christian, The crystallography of martensitic transformations, J. Iron Steel Inst. 197 (1961) 122–131.
[25] A.H. Zahiri, J. Ombogo, L. Cao, Formation of $\{11\bar{2}2\}$ contraction twins in titanium through reversible martensitic phase transformation, Scr. Mater. 195 (2021) 113694.
[26] J. Ombogo, A.H. Zahiri, T. Ma, L. Cao, Nucleation of $\{10\bar{1}2\}$ twins in magnesium through reversible martensitic phase transformation, Metals 10 (8) (2020) 1030.
[27] A.H. Zahiri, J. Ombogo, T. Ma, P. Chakraborty, L. Cao, Transformation-induced plasticity in omega titanium, J. Appl. Phys. 129 (1) (2021) 015105.
[28] P. Chen, F. Wang, B. Li, Transitory phase transformations during $\{10\bar{1}2\}$ twinning in titanium, Acta Mater. 171 (2019) 65–78.
[29] Y. Gao, Y. Zhang, B.W. Beeler, Y. Wang, Self-organized multigrain patterning with special grain boundaries produced by phase transformation cycling, Phys. Rev. Mater. 2 (7) (2018) 073402.
[30] Y. Gao, J.-H. Ke, B. Mao, Y. Liao, Y. Zheng, L.K. Aagesen, Twinning path determined by broken symmetry: arevisit to deformation twinning in hexagonal close-packed titanium and zirconium, Phys. Rev. Mater. 4 (7) (2020) 070601.
[31] Z. Nishiyama, M. Oka, H. Nakagawa, $\{10\bar{1}1\}$ transformation twins in titanium, Trans. Jpn. Inst. Metals 7 (3) (1966) 174–177.
[32] P. Gaunt, J. Christian, The crystallography of the β-α transformation in zirconium and in two titanium-molybdenum alloys, Acta Metall. 7 (8) (1959) 534–543.
[33] J. Mackenzie, J. Bowles, The crystallography of martensite transformations—IV body-centred cubic to orthorhombic transformations, Acta Metall. 5 (3) (1957) 137–149.
[34] S. Plimpton, Fast Parallel Algorithms for Short-Range Molecular Dynamics, J. Chem. Phys. 117 (1) (1995) 1–19, doi:10.1006/jcph.1995.1039.
[35] M.I. Mendelev, T.L. Underwood, G.J. Ackland, Development of an interatomic potential for the simulation of defects, plasticity, and phase transformations in titanium, J. Chem. Phys. 145 (15) (2016) 154102.
[36] D.J. Evans, B.L. Holian, The nose hoover thermostat, J. Chem. Phys. 83 (8) (1985) 4069–4074, doi:10.1063/1.449071. https://doi.org/10.1063/1.449071.
[37] M. Parrinello, A. Rahman, Polymorphic transitions in single crystals: a new molecular dynamics method, J. Appl. Phys. 52 (12) (1981) 7182–7190.
[38] A.H. Zahiri, L. Carneiro, J. Ombogo, P. Chakraborty, L. Cao, On the formation of $\{11\bar{2}2\}$ boundary via $\{10\bar{1}2\}$-$\{01\bar{1}2\}$ twin–twin interaction in magnesium, Comput. Mater. Sci 201 (2022) 110887.
[39] A. Stukowski, Visualization and analysis of atomistic simulation data with OVITO–the open visualization tool, Model. Simul. Mater. Sci. Eng. 18 (1) (2009) 015012, doi:10.1088/0965-0393/18/1/015012. https://doi.org/10.1088%2F0965-0393%2F18%2F1%2F015012.
[40] D. Faken, H. Jnsson, Systematic analysis of local atomic structure combined with 3D computer graphics, Comput. Mater. Sci 2 (2) (1994) 279–286.
[41] J.D. Honeycutt, H.C. Andersen, Molecular dynamics study of melting and freezing of small Lennard–Jones clusters, J. Phys. Chem. 91 (19) (1987) 4950–4963.
[42] R.M. Wood, The lattice constants of high purity alpha titanium, Proc. Phys. Soc. 80 (3) (1962) 783–786, doi:10.1088/0370-1328/80/3/323. https://doi.org/10.1088/0370-1328/80/3/323
[43] C. Baruffi, A. Finel, Y. Le Bouar, B. Bacroix, O.U. Salman, Atomistic simulation of martensite microstructural evolution during temperature driven $\beta\alpha$ transition in pure titanium, Comput. Mater. Sci 203 (2022) 111057.
[44] E. Vitral, J.A. Hanna, Quadratic-stretch elasticity, Math. Mech. Solids 27 (3) (2022) 462–473.
[45] Y. Gao, Y. Zhang, Y. Wang, Determination of twinning path from broken symmetry: a revisit to deformation twinning in bcc metals, Acta Mater. 196 (2020) 280–294.
[46] A. Crocker, M. Bevis, The crystallography of deformation twinning in titanium, in: R. Jaffee, N. Promisel (Eds.), The Science, Technology and Application of Titanium, Pergamon, 1970, pp. 453–458.
[47] R.E. Reed-Hill, J.P. Hirth, H.C. Rogers, Deformation Twinning: Proceedings of a Conference Sponsored by the Metallurgical Society, American Institute of Mining, Metallurgical, and Petroleum Engineers and the College of Engineering, University of Florida in Cooperation with the Florida Institute for Continuing University Studies: Gainesville, Fla., March 21-22, 1963, 1964.
[48] A. Crocker, The role of twinning in martensite transformations, in: R.E. Reed-Hill, J.P. Hirth, H.C. Rogers (Eds.), Conference on Deformation Twinning, Gainesville, FL, Deformation Twinning, vol. 25, Blackie: Gordon and Breach Science Publishers, 1964, pp. 272–294.
[49] J.W. Christian, S. Mahajan, Deformation twinning, Prog. Mater. Sci. 39 (1–2) (1995) 1–157.
[50] J.M. Ball, R.D. James, Fine phase mixtures as minimizers of energy, Arch. Ration. Mech. Anal. 100 (1) (1987) 13–52.
[51] K. Bhattacharya, Microstructure of Martensite: Why it Forms and How it Gives Rise to the Shape-memory Effect, vol. 2, Oxford University Press, 2003.